RSC Applied Interfaces

ROYAL SOCIETY OF CHEMISTRY

COMMUNICATION

View Article Online
View Journal | View Issue

Cite this: *RSC Appl. Interfaces*, 2025, **2**, 1586

Received 29th July 2025,
Accepted 9th September 2025

DOI: 10.1039/d5lf00217f

rsc.li/RSCApplInter

Voltage-dependent time constants for neuromorphic organic electrochemical transistor applications

Shunsuke Yamamoto, *[ab] Nanako Kanazumi[a] and Masaya Mitsuishi [a]

Organic electrochemical transistors (OECTs) with neuromorphic functions were developed using layer-by-layer ferrocene coatings on PEDOT:PSS. The ferrocene unit density increased proportionally with more layers. Neuromorphic behavior, including synapse plasticity, was controlled *via* gate voltages linked to capacitive or redox processes. This approach offers promising flexibility for programmable neuromorphic device design.

As the demand for adaptive and low-power electronics grows, organic electrochemical transistors (OECTs) are attracting increasing attention for neuromorphic applications. OECTs operate by ion injection and extraction in organic mixed conductor-based channels,[1–5] a process that closely resembles neural signal transmission. This similarity makes them highly promising for neuromorphic device applications.[6–12] The function of such devices depends on ionic processes with asymmetric time constants, where ion injection and extraction occur at different rates. Several designs have demonstrated neuromimetic behavior by trapping injected ions to significantly delay the extraction time.[13] Conversely, accelerating ionic dynamics has been reported to decrease the time constant of neuromorphic operations. A common technique for speed-tuning is the addition of a third component to a mixed conductor.[10,11,14] For instance, poly(ethers), such as polytetrahydrofuran, trap alkali metal ions in the film to realize large hysteresis in device operation,[14] whereas poly(styrene sulfonate) sodium salt (PSSNa) facilitates ion movement for faster operation.[11] These methodologies remain the focus of research as potential means of streamlining manufacturing processes.

While previous studies have enabled control over synaptic-like time constants during the fabrication process, adjusting these constants at the post-fabrication stage remains a major challenge for neuromorphic device development. Achieving such post-fabrication programmability would offer greater flexibility in designing and building organic neural networks. One way to achieve such programmability is to incorporate molecules with multiple thermodynamically stable states into the device. This concept, used in memory devices like floating-gate transistors,[15,16] and atomic switches,[17,18] enables bistable switching but typically requires ionic diffusion for neuromorphic function. Here, we realize a similar structure by placing bistable molecules on an OECT channel coated with an ultrathin insulating layer.

In this study, we developed OECTs incorporating redox-active layer-by-layer (LbL) films to achieve programmable retention behavior. Our previous work showed that ferrocene-modified polyethyleneimine (PEI-Fc)-based LbL films (Fig. 1a and b) can function as resistive switching devices.[19] Building on this, we integrate the LbL films on PEDOT:PSS in a three-terminal OECT architecture: PEDOT:PSS|PEI-Fc/PSS LbL films (Fig. 1c). In contrast to earlier studies that focused on controlling ion permeation,[20–22] this approach leverages redox activity to modulate synaptic plasticity.

Fig. 2 illustrates the UV-vis spectra obtained during the LbL cycles to confirm uniform deposition. The absorption peak at 227 nm was ascribed to the π–π* transition of benzene rings in PSS,[23,24] which served as a good indicator of the deposition quality of the LbL layers. UV-vis measurements are performed on PEDOT:PSS and bare quartz substrate. As reported in our previous study,[24] green and orange dots exhibit linear trends for PEI with and without

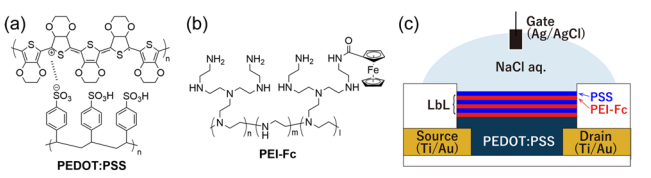

Fig. 1 (a and b) Chemical structures of polymers and (c) schematic illustration of ferrocene-functionalized OECT devices based on PEDOT:PSS|PEI-Fc/PSS LbL films.

[a] *Graduate School of Engineering, Tohoku University, 6-6-11 Aramaki Aza Aoba, Aoba-ku, Sendai 980-8579, Japan*
[b] *Graduate School of Engineering, Kyoto University, Katsura, Nishikyo-ku, Kyoto 615-8510, Japan. E-mail: syama@photo.polym.kyoto-u.ac.jp*

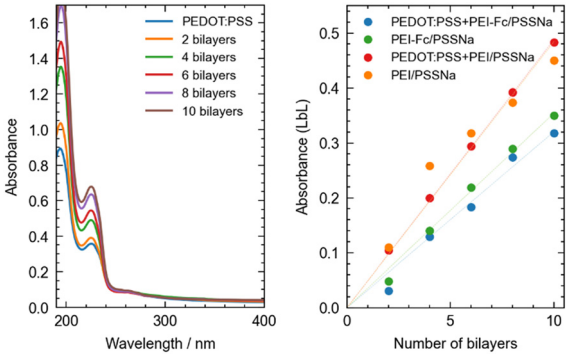

Fig. 2 UV-vis absorption spectroscopy data of PEDOT:PSS and PEDOT:PSS|PEI-Fc/PSS LbL films; (Left) spectra and (Right) development of absorption at 227 nm for LbL films on PEDOT:PSS films or quartz substrates. Note that the contribution from the underlying PEDOT:PSS layer was subtracted to isolate the absorbance of the LbL overlayer.

ferrocene moieties, respectively, confirming uniform deposition on quartz substrates. The red and blue dots show the trends of the samples on the PEDOT:PSS films. Each case exhibited linear trends with the number of bilayers up to 10, indicating a uniform deposition on the PEDOT:PSS film. Notably, the slopes of the PEI-Fc samples were slightly smaller than those of the samples without ferrocene units. This finding might be attributed to the reduction in charge on the PEI chains owing to the functionalization by the ferrocene units. In addition, water contact angle measurements were carried out after each deposition cycle. The contact angle exhibited periodic changes corresponding to the sequential adsorption of PSS and PEI-Fc, confirming the multilayered architecture of the films with interpenetrated structures (see SI). These results demonstrated that the functionalized PEI-Fc was uniformly deposited on the PEDOT:PSS substrates *via* the LbL method.

Fig. 3 shows the CV data for the PEDOT:PSS|PEI-Fc/PSS LbL films. In the control experiment for the samples with PEI and PSS bilayers, the LbL films without Fc exhibited capacitive behavior, which was observed as a square-shaped voltammogram. In contrast, the PEI-Fc/PSS samples exhibited additional redox peaks at a gate voltage of approximately −370 mV. These reversible peaks were assignable to the redox reactions of the ferrocene units.[25] To confirm whether the redox-active ferrocene units were bound to the substrate, the scan rate dependence of the peak currents was examined for each sample with different layer numbers. The right panel of Fig. 3 shows the plot, and all cases follow a power of one to the scan rate, indicating that the redox-active ferrocene moieties are bound to the substrate and do not diffuse into the electrolyte.[26] The effective surface density of Fc was calculated from the slopes of these lines using the following equation:

$$I_p = n^2F^2\nu A\Gamma/(4RT) \quad (1)$$

where n, F, ν, A, Γ, R, and T are the number of electrons in the redox reaction (n = 1), the Faraday constant, scan rate, sample area, surface density of the redox-active species, gas constant, and temperature, respectively. The Γ values were determined to be 3.97×10^{-11}, 6.96×10^{-11}, and 9.55×10^{-11} mol cm^{-2} for the samples with two, four, and six bilayers, respectively. These values were proportional to the number of layers (Γ per layer $\Gamma^* = 1.67 \times 10^{-11}$ mol cm^{-2} per layer). This result indicates that most of the ferrocene units in the LbL films were redox-active in the film state. Note that the Γ^* on PEDOT:PSS layer is slightly larger than our previous work on bare ITO substrates,[19] suggesting the improved electrical connections due to interpenetration between the LbL layer and the PEDOT:PSS layer. In summary, the PEI-Fc/PSS LbL systems were prepared on the PEDOT:PSS films while maintaining the redox activity of the ferrocene moieties.

The ferrocene-functionalized films were incorporated into the OECT devices based on the fundamental analysis described above. Fig. 4 shows the output and transfer curves of the OECT devices. The output curve demonstrates depression-mode operation, where the drain current decreases upon applying a gate bias. These operations were similar to those of the neat PEDOT:PSS film, suggesting that

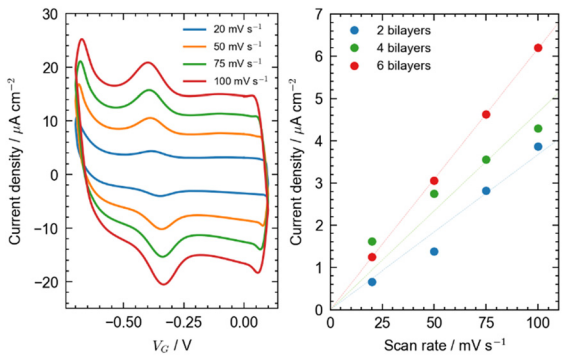

Fig. 3 Cyclic voltammetry data for PEDOT:PSS|PEI-Fc/PSS samples: (Left) cyclic voltammogram for six-bilayer sample and (Right) peak current *vs.* scan rate plot. The horizontal axis in the left panel shows the gate voltage, which is reversed relative to the standard electrochemical representation (*vs.* Ag/AgCl).

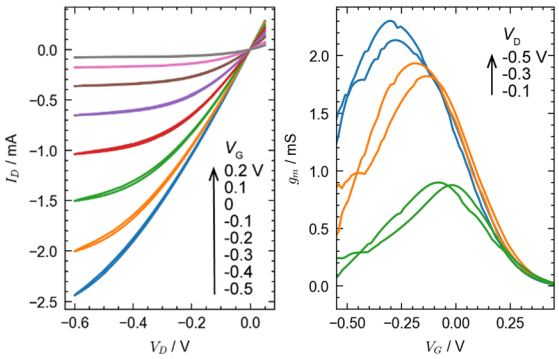

Fig. 4 Output and transfer characteristics of an organic electrochemical transistor (OECT) using PEDOT:PSS|PEI-Fc/PSS films (6 cycles). Output curves are recorded at V_G = +0.2, +0.1, …, −0.5 V, and transfer curves are shown at V_D = −0.1, −0.3, and −0.5 V. All measurements were conducted in 0.1 M NaCl aqueous solution using an Ag/AgCl pellet as the gate electrode.

cations in the electrolyte were injected into and extracted from the channel layer through the LbL layer. A small hysteresis in the output and transfer curves further supported ion penetration into the LbL layer. The maximum value of the transconductance g_m of the ferrocene-functionalized device was 2.3 mS at V_D = −0.5 V, which was *ca.* 20% of that of the OECT based on neat PEDOT:PSS (12 mS at V_D = −0.5 V, see SI). According to the OECT device model, in which the transconductance is proportional to the product of the hole mobility and volumetric capacitance μC^*, this reduction is attributed to the decrease in the effective capacitance of the PEDOT:PSS layer underneath the PEI-Fc/PSS LbL layer.[1–5] Although the capacitance of this underlying PEDOT:PSS layer could not be directly extracted, comparative CV measurements of PEDOT:PSS coated with PEI/PSS and PEI-Fc/PSS LbL layers revealed nearly constant total capacitance irrespective of the number of deposition cycles (see SI). This indicates that while the overall capacitance remains unchanged, the effective contribution from the PEDOT:PSS base layer is reduced when the redox-active LbL films are deposited. These results indicated the suitability of LbL deposition for neuromorphic devices without affecting OECT properties. Furthermore, control devices based on PEDOT:PSS, PEDOT:PSS/PSS, and PEDOT:PSS|PEI/PSS exhibited negligible hysteresis in their output and transfer curves (see SI), in contrast to the pronounced hysteresis observed for the PEDOT:PSS|PEI-Fc/PSS devices. This hysteresis arises from the redox activity of the ferrocene moieties and represents a unique advantage of the ferrocene-functionalized films for achieving programmable synaptic plasticity.

Neuromorphic operations of the OECT devices were tested using pair-pulsed depression (PPD) test. In this test, a voltage pulse train was applied to the gate electrode with varying intervals (Δt), and the transient drain currents were recorded. At a gate voltage of +0.2 V, where only capacitive processes dominate (as indicated in Fig. 4), the PPD behavior is consistent with conventional PEDOT:PSS-based devices or their blends with PSS-Na.[10,11] In this case, A_1 and A_2 differ due to slow ion extraction and cumulative de-doping, as shown in Fig. 5. This response follows a single exponential decay with a time constant $\tau \approx 60$ ms, reflecting the typical ion-shuttling mechanism. Such PPD behavior has been widely observed in pristine PEDOT:PSS systems.[11] To further improve ionic transport, PEDOT:PSS channel layer modifications have been explored. Among them, Nafion incorporation has been demonstrated with enhanced paired-pulse facilitation because of effective ion penetration.[27] However, in both pristine and Nafion-modified systems, the characteristic time constants remain essentially independent of the applied gate bias. In contrast, the ferrocene-modified PEDOT:PSS|PEI-Fc/PSS devices presented here not only retain PPD but also exhibit a clear gate-voltage-dependent modulation of the decay time constant, highlighting a unique functional advantage of the ferrocene incorporation. When a gate voltage is applied that activates the redox reaction of the ferrocene moieties (V_G = −0.4 V), the PPD behavior changes

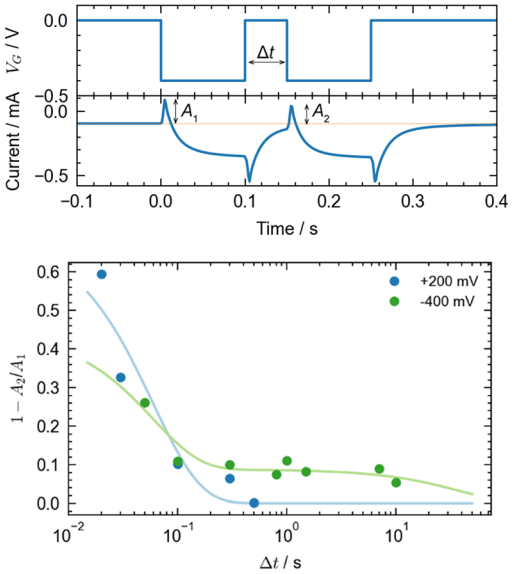

Fig. 5 Paired-pulse-depression (PPD) in PEDOT:PSS|PEI-Fc/PSS OECTs. (Top) Applied voltage stimulus at gate with pulse interval of Δt = 50 ms, pulse amplitude of −0.5 V, and pulse width of 100 ms, leading to drain current transients measured at a constant drain voltage of V_D = −0.5 V. Time zero corresponds to the onset of the first gate pulse. The peak drain current amplitudes immediately after the first and second gate pulses were defined as A_1 and A_2, respectively (indicated by arrows). (Bottom) Depression in drain current amplitude from baseline (A_1 and A_2) as a function of pulse interval Δt for a OECT device operated at different gate pulse amplitude. Solid lines represent exponential fits to the data: a single-exponential function for +200 mV, and a two-component exponential function for −400 mV. For the −400 mV condition, τ_2 = 30 s was obtained from curve fitting; however, as this value approaches the maximum Δt in the experiment, it should be regarded as a lower bound.

significantly. The redox switching between two thermodynamically stable states introduces a different response profile. As summarized in Fig. 5, the device nonlinearity, evaluated as $1 - A_2/A_1$, shows clear voltage dependence. Under redox-active conditions, the decay kinetics require a two-component exponential fit, suggesting distinct contributions from capacitive and redox processes. Notably, the first component ($\tau_1 \approx 60$ ms) matches the time constant observed at V_G = −0.2 V, suggesting that this component corresponds to capacitive ion injection and extraction. The second, slower component is therefore attributed to the redox process of the ferrocene moieties. This component exhibits a time constant of $\tau_2 > 30$ s (note that this reflects the upper limit of Δt accessible in our measurement setup), corresponding to the reduction of Fc^+ to Fc, which is limited by electron transfer due to the low ferrocene content.

In our previous study, we reported that the apparent hole diffusion constant (D_{app}) was of the order of 10^{-14} to 10^{-15} cm^2 s^{-1}, indicating that hole diffusion proceeded by the polymer segment motion mechanism.[19] Based on this value, the calculated diffusion length during τ_2 under one-dimensional diffusion was $\sqrt{D_{app}\tau_2} \sim 10^1$ nm, which was

consistent with the thickness of the LbL film. This finding supports the hypothesis that the slow component originates from an Fc^+/Fc redox reaction. From a practical standpoint, this voltage-dependent behavior can be used to mimic synaptic plasticity in a single device by simply changing the polarity of the gate voltage. The presence of a slower decay component ($\tau_2 > 30$ s) under redox-active conditions further indicates that the retention characteristics of the device can be extended beyond the typical short-term range, potentially enabling multiscale synaptic response behavior. This feature is advantageous for controlling the response speed of the neuromorphic OECT devices. Further optimization and mechanistic investigations will pave the way for programmable neuromorphic devices and circuits based on OECTs.

Conclusions

This study demonstrated the successful LbL deposition of ferrocene-containing polyelectrolytes (PEI-Fc/PSS) onto the PEDOT:PSS films under ambient conditions. The deposition cycles were monitored using water contact angle measurements, UV-vis spectroscopy, and cyclic voltammetry to demonstrate the uniformity and functionality of the film. The OECT device based on the ferrocene-functionalized films of PEDOT:PSS and PEI-Fc/PSS LbL building blocks operated under the depression mode without compromising the integrity of the underlying PEDOT:PSS layer. The PPD test demonstrated the ability to control the time constants by adjusting the gate voltage polarity, mimicking the synaptic plasticity processes observed in biological neurons. This study presents a novel approach for voltage-dependent programmability in OECT-based neuromorphic systems by incorporating redox-active LbL films. Beyond mimicking synaptic behavior, the method offers a pathway toward neuromorphic circuits with tunable memory and response speed, expanding the design flexibility for organic artificial neural systems.

Author contributions

SY designed and conceived the experiments with help from NK and MM. NK fabricated and characterized the devices. NK and SY analysed data obtained. The manuscript was written with contributions from all authors. All authors have given approval to the final version of the manuscript.

Conflicts of interest

There are no conflicts to declare.

Data availability

Supplementary information: Methods, results on water contact angle measurements, and performance of PEDOT:PSS OECT devices. See DOI: **https://doi.org/10.1039/D5LF00217F**.

The data supporting this article have been included as part of the SI.

Acknowledgements

We thank Mr. Shunsuke Kayamori, Instrumental Analysis Group, Technical Division, Graduate School of Engineering, Tohoku University, for ICP-AES measurements. This research was supported by JSPS KAKENHI Grant Numbers JP21H01992 and JP24K01542, funded by the Tateishi Science and Technology Foundation, the Toyota Physical and Chemical Research Institute, and the Suzuki Foundation.

References

1 J. Rivnay, S. Inal, A. Salleo, R. M. Owens, M. Berggren and G. G. Malliaras, *Nat. Rev. Mater.*, 2018, **3**, 17086.
2 B. D. Paulsen, K. Tybrandt, E. Stavrinidou and J. Rivnay, *Nat. Mater.*, 2019, **19**, 13–26.
3 N. A. Kukhta, A. Marks and C. K. Luscombe, *Chem. Rev.*, 2022, **122**, 4325–4555.
4 D. Ohayon, V. Druet and S. Inal, *Chem. Soc. Rev.*, 2023, **52**, 1001–1023.
5 Y. Wang, S. Wustoni, J. Surgailis, Y. Zhong, A. Koklu and S. Inal, *Nat. Rev. Mater.*, 2024, **9**, 249–265.
6 P. Gkoupidenis, N. Schaefer, B. Garlan and G. G. Malliaras, *Adv. Mater.*, 2015, **27**, 7176–7180.
7 Y. Van De Burgt, A. Melianas, S. T. Keene, G. G. Malliaras and A. Salleo, *Nat. Electron.*, 2018, **1**, 386–397.
8 S. Pecqueur, M. Mastropasqua Talamo, D. Guérin, P. Blanchard, J. Roncali, D. Vuillaume and F. Alibart, *Adv. Electron. Mater.*, 2018, **4**, 1800166.
9 T. N. Mangoma, S. Yamamoto, G. G. Malliaras and R. Daly, *Adv. Mater. Technol.*, 2020, **7**, 2000798.
10 S. Yamamoto and G. G. Malliaras, *ACS Appl. Electron. Mater.*, 2020, **2**, 2224–2228.
11 S. Yamamoto, A. G. Polyravas, S. Han and G. G. Malliaras, *Adv. Electron. Mater.*, 2022, **8**, 2101186.
12 Z. Laswick, X. Wu, A. Surendran, Z. Zhou, X. Ji, G. M. Matrone, W. L. Leong and J. Rivnay, *Nat. Commun.*, 2024, **15**, 6309.
13 X. Ji, B. D. Paulsen, G. K. K. Chik, R. Wu, Y. Yin, P. K. L. Chan and J. Rivnay, *Nat. Commun.*, 2021, **12**, 2480.
14 B. Winther-Jensen, B. Kolodziejczyk and O. Winther-Jensen, *APL Mater.*, 2015, **3**, 014903.
15 M. Kang, K.-J. Baeg, D. Khim, Y.-Y. Noh and D.-Y. Kim, *Adv. Funct. Mater.*, 2013, **23**, 3503–3512.
16 R. Wang, P. Chen, D. Hao, J. Zhang, Q. Shi, D. Liu, L. Li, L. Xiong, J. Zhou and J. Huang, *ACS Appl. Mater. Interfaces*, 2021, **13**, 43144–43154.
17 B. J. Choi, D. S. Jeong, S. K. Kim, C. Rohde, S. Choi, J. H. Oh, H. J. Kim, C. S. Hwang, K. Szot, R. Waser, B. Reichenberg and S. Tiedke, *J. Appl. Phys.*, 2005, **98**, 033715.
18 A. Nayak, T. Ohno, T. Tsuruoka, K. Terabe, T. Hasegawa, J. K. Gimzewski and M. Aono, *Adv. Funct. Mater.*, 2012, **22**, 3606–3613.

19 Y. Ishizaki, A. Watanabe, S. Yamamoto and M. Mitsuishi, *ACS Appl. Electron. Mater.*, 2023, **5**, 3957–3964.
20 A. M. Pappa, S. Inal, K. Roy, Y. Zhang, C. Pitsalidis, A. Hama, J. Pas, G. G. Malliaras and R. M. Owens, *ACS Appl. Mater. Interfaces*, 2017, **9**, 10427–10434.
21 G. E. Fenoy, J. Scotto, J. A. Allegretto, E. Piccinini, A. L. Cantillo, W. Knoll, O. Azzaroni and W. A. Marmisollé, *ACS Appl. Electron. Mater.*, 2022, **4**, 5953–5962.
22 J. F. Diforti, E. Piccinini, J. A. Allegretto, C. von Bilderling, W. A. Marmisollé and O. Azzaroni, *ACS Appl. Electron. Mater.*, 2024, **6**, 1211–1222.
23 S. Yamamoto, R. Miyako, R. Maeda, Y. Ishizaki and M. Mitsuishi, *Macromol. Mater. Eng.*, 2023, **308**, 2300247.
24 C. De Saint-Aubin, J. Hemmerlé, F. Boulmedais, M. F. Vallat, M. Nardin and P. Schaaf, *Langmuir*, 2012, **28**, 8681–8691.
25 A. Paul, R. Borrelli, H. Bouyanfif, S. Gottis and F. Sauvage, *ACS Omega*, 2019, **4**, 14780–14789.
26 A. J. Bard, R. L. Faulkner and H. S. White, *Electrochemical Methods: Fundamentals and Applications*, 3rd edn, Wiley, 2022.
27 Y. J. Lee, Y. H. Kim and E. K. Lee, *Macromol. Rapid Commun.*, 2024, **45**, 2400165.